Available online at www.sciencedirect.com
SCIENCE DIRECT®
Composites Science and Technology 63 (2003) 1671–1687
COMPOSITES SCIENCE AND TECHNOLOGY
www.elsevier.com/locate/compscitech

Constitutive modeling of nanotube–reinforced polymer composites

G.M. Odegard[a,*], T.S. Gates[b], K.E. Wise[a], C. Park[a], E.J. Siochi[c]

[a]National Institute of Aerospace, NASA Langley Research Center, MS 390, Hampton, VA, 23681, USA
[b]NASA Langley Research Center, MS 188E, Hampton, VA, 23681, USA
[c]NASA Langley Research Center, MS 226, Hampton, VA, 23681, USA

Received 16 August 2002; received in revised form 16 September 2002; accepted 15 December 2002

Abstract

In this study, a technique is presented for developing constitutive models for polymer composite systems reinforced with single-walled carbon nanotubes (SWNT). Because the polymer molecules are on the same size scale as the nanotubes, the interaction at the polymer/nanotube interface is highly dependent on the local molecular structure and bonding. At these small length scales, the lattice structures of the nanotube and polymer chains cannot be considered continuous, and the bulk mechanical properties can no longer be determined through traditional micromechanical approaches that are formulated by using continuum mechanics. It is proposed herein that the nanotube, the local polymer near the nanotube, and the nanotube/polymer interface can be modeled as an effective continuum fiber by using an equivalent-continuum modeling method. The effective fiber serves as a means for incorporating micromechanical analyses for the prediction of bulk mechanical properties of SWNT/polymer composites with various nanotube lengths, concentrations, and orientations. As an example, the proposed approach is used for the constitutive modeling of two SWNT/polyimide composite systems.
Published by Elsevier Ltd.

Keywords: B. Mechanical properties; B. Modelling; C. Anisotropy; Carbon nanotubes; Nanotechnology

1. Introduction

In recent years, nano-structured, non-metallic materials have spurred considerable interest in the materials community partly because of their potential for large gains in mechanical and physical properties as compared to standard structural materials. In particular, carbon nanotube/polymer composites may provide order-of-magnitude increases in strength and stiffness when compared to typical carbon fiber/polymer composites. In order to facilitate the development of nanotube-reinforced polymer composites, constitutive relationships must be developed that predict the bulk mechanical properties of the composite as a function of molecular structure of the polymer, nanotube, and polymer/nanotube interface.

For computational simplicity, and to adequately address scale-up issues, it is desirable to couple an equivalent-continuum model of a nanotube/polymer composite with established micromechanical models to describe the mechanical behavior. As outlined by McCullough [1,2], numerous micromechanical models have been developed to predict the macroscopic behavior of polymeric composite materials reinforced with typical reinforcement such as carbon or glass fibers. These micromechanical models assume that the fiber, matrix, and sometimes, the interface, are continuous materials and the constitutive equations for the bulk composite material are formulated based on assumptions of continuum mechanics. However, for nanostructured materials, such as nanotube-reinforced polymers, a typical single-walled nanotube (SWNT) may have a diameter of approximately $1–10\times10^{-9}$ m, compared to the typical carbon-fiber diameter of 50×10^{-6} m, which leads to a breakdown of the rules and requirements for continuum modeling. Even though a limited number of studies have attempted to address the applicability of continuum micromechanics to nanotube-reinforced polymer composites [3,4], it appears that the direct use of micromechanics for nanotube composites is inappropriate without taking into account the effects associated with the significant size difference between a nanotube and a typical carbon fiber, as described below.

To help address this analysis deficiency, atomistic simulation can be used to investigate behavior of

* Corresponding author. Tel.: +1-757-864-2759.
E-mail address: g.m.odegard@larc.nasa.gov (G.M. Odegard).

0266-3538/03/$ - see front matter Published by Elsevier Ltd.
doi:10.1016/S0266-3538(03)00063-0

Nomenclature

Molecular model

a	bond number
D_a^{IJ}	well depth of interaction a involving atoms I and J
K_a^{θ}	angle variance force constant
K_a^{ρ}	stretching force constant
Λ^{m}	total molecular potential energy
θ_a	deformed bond-angle number a
Θ_a	undeformed bond-angle number a
ρ_a	deformed interatomic distance of bond number a
ρ_a^{IJ}	Van der Waals distance for interaction a involving atoms I and J
P_a	undeformed interatomic distance of bond number a

Equivalent-truss model

A_a^b	cross-sectional area of rod a of truss member type b
r_a^b	deformed lengths of rod a of truss member type b
R_a^b	undeformed lengths of rod a of truss member type b
Y_a^b	Young's modulus of rod a of truss member type b
α	bond-stretching interaction truss member type
β	bond-angle variance interaction truss member type
Λ^t	total strain energy of truss model
ω	Van der Waals interaction truss member type

Equivalent-continuum model and composite

$\mathbf{A}^f$	dilute mechanical strain concentration tensor of effective fiber
c_{ij}	direction cosines for coordinate transformation
$\mathbf{C}$	elastic stiffness tensor of the composite
C_{ijkl}^f, C_{ij}^f, $\mathbf{C}^f$	elastic stiffness tensor of effective fiber
$\mathbf{C}^m$	elastic stiffness tensor of matrix
D	diameter of effective fiber
e	applied strain magnitude
E	Young's modulus of isotropic composite
E_{L}	longitudinal Young's modulus of composite
E_{T}	transverse Young's modulus of anisotropic composite
E_{L}^f	longitudinal Young's modulus of effective fiber
G	shear modulus of isotropic composite
G_{L}	longitudinal shear modulus of anisotropic composite
G_{L}^f	longitudinal shear modulus of effective fiber
G_{T}^f	transverse shear modulus of effective fiber
$\mathbf{I}$	identity tensor
k	axisymmetric alignment factor
K_{T}^f	transverse bulk modulus of effective fiber
L	length of effective fiber
n_j	outward normal to boundary B
s_1, s_2	orientation factors
$\mathbf{S}$	Eshelby's tensor
$T_i(B)$	tractions applied onto boundary B
$u_i(B)$	displacements applied onto boundary B
v_f	effective fiber volume fraction
v_m	matrix volume fraction
V	volume of effective fiber
x_j	coordinate system of effective fiber
x_j'''	global coordinate system
ε_{kl}	strain tensor
$\delta(y-\bar{y})$	Dirac delta distribution centered at $\bar{y}$
ϕ, ψ, γ	angles of coordinate transformation
$\lambda(\phi,\psi)$	orientation distribution function
Λ^f	total strain energy of effective fiber
σ_{ij}	stress tensor

materials at the nanometer length scale. Recently, Wise and Hinkley [5] used molecular dynamics simulations to address the polymer/SWNT material response for a SWNT surrounded by polyethylene molecules. They predicted that the local changes in the polymer molecular structure and the non-functionalized polymer/SWNT interface are on the same length scale as the width of the nanotube. The magnitude of this localized effect is generally unknown and needs to be accurately modeled to ensure that the full load-transfer capabilities of the polymer/SWNT composite are accounted for in both bulk stiffness and strength calculations.

The first step towards calculation of bulk stiffness and strength is to establish a constitutive model that can be used in a continuum mechanics formulation. The continuum model must account for the fundamental assumption in continuum mechanics that the mass, momentum, and energy can be represented in a mathematical sense by continuous functions, that is, independent of length scale.

In this paper, a technique for developing constitutive models for SWNT-reinforced polymer composite materials is proposed which is based on the equivalent-continuum modeling technique for nano-structured materials which was developed by Odegard et al. [6]. The modeling technique takes into account the discrete nature of the atomic interactions at the nanometer length scale and the interfacial characteristics of the nanotube and the surrounding polymer matrix. After the constituent materials used in this paper are discussed in detail, the development of the constitutive model using the presented technique is described. First, a model of the molecular structure of the nanotube and the adjacent polymer chains is established by using the atomic structure that has been determined from molecular dynamics (MD) simulations. Second, an equivalent-continuum model is developed in which the mechanical properties are determined based on the force constants that describe the bonded and non-bonded interactions of the atoms in the molecular model and reflect the local polymer and nanotube structure. Finally, the equivalent-continuum model is used in micromechanical analyses to determine the bulk constitutive properties of the SWNT/polymer composite with aligned and random nanotube orientations and with various nanotube lengths and volume fractions. In addition, predicted values of modulus are compared with experimental data obtained from mechanical testing.

2. Constituent materials

The constitutive models developed in this study are for SWNT/polyimide composites with a PmPV interface. The properties of the constituent materials are described first.

2.1. Carbon nanotube

In 1991 Iijima [7] obtained transmission electron micrographs of elongated, nano-sized carbon particles that consisted of cylindrical graphitic layers, known today as carbon nanotubes. Because of their high inter-atomic bond strength and perfect lattice structure, a Young's modulus as high as 1 TPa and a tensile strength approaching 100 GPa have been measured for single-walled carbon nanotubes (SWNT) [8]. These properties, in addition to their relatively low density, make SWNT an ideal candidate as a reinforcing constituent. For this study, a (6,6) (see Ref. [9] for an explanation of this notation), straight, finite-length, single-walled carbon nanotube is modeled.

2.2. Nanotube/polymer interface

Accurate representation of the nanotube-to-polymer interface is essential for modeling nano-scale structure–property relationships. In a recent molecular dynamics study of SWNT/polymer materials, Frankland et al. [10] addressed the effects of covalent bonds at the SWNT/polymer interface. They have shown that for nanotube/polyethylene composites there is a one to two order-of-magnitude increase in the interfacial shear strength for composites with covalent bonding between the nanotube and adjacent polymer molecules, relative to systems without the covalent bonds. However, other studies [11,12] have shown that because the covalent bonding may significantly affect the properties of the nanotube itself, it is desirable to increase the load transfer between the nanotube and polymer by using improved non-covalent bonding methods. For example, it has been shown that PmPV molecules [poly(*m*-phenylenevinylene) substituted with octyloxy chains] naturally wrap around carbon nanotubes in a helical pattern [12]. This wrapping allows for an improved nanotube/polymer molecule interaction through non-covalent bonded interactions, and thus improved load transfer at the nanotube/polymer interface, compared to those found with most structural polymers. Because the PmPV polymer molecules will likely entangle themselves with neighboring structural polymer molecules (such as polyimides), the PmPV can be used as a highly effective interface between the nanotube and structural polymer, and is used as the interface in the present study. The molecular structure of a single unit of the PmPV molecule is shown in Fig. 1. The subscripts on the atomic labels in Fig. 1 correspond to the subscripts shown in Tables 1–3, which are discussed below.

2.3. Polymer matrix

The nanotubes used in this study are assumed to be well dispersed inside a bulk polymer matrix. Two polymers were considered in the present study. The first polymer considered is LaRC-SI, a thermoplastic polyimide that has been shown to have good mechanical properties for various processing and testing conditions [13–16]. The properties of LaRC-SI used in this study have been taken from Whitley et al. [16] for the system with a 3% stoichiometric imbalance at room temperature. The Young's modulus and Poisson's ratio of this material are 3.8 GPa and 0.4, respectively.

The second polymer considered in this study is the colorless polyimide LaRC-CP2 [17]. This optically transparent polyimide is resistant to radiation and may be used to make thin polymer films for building large space structures. The mechanical properties of this polymer are not known a priori, and have been experimentally determined as described in Section 7.2.

In order to synthesize the nanotube/LaRC-CP2 composite, a batch of purified laser-ablated SWNTs was obtained from Rice University, and transmission electron microscope (TEM) and atomic force microscope

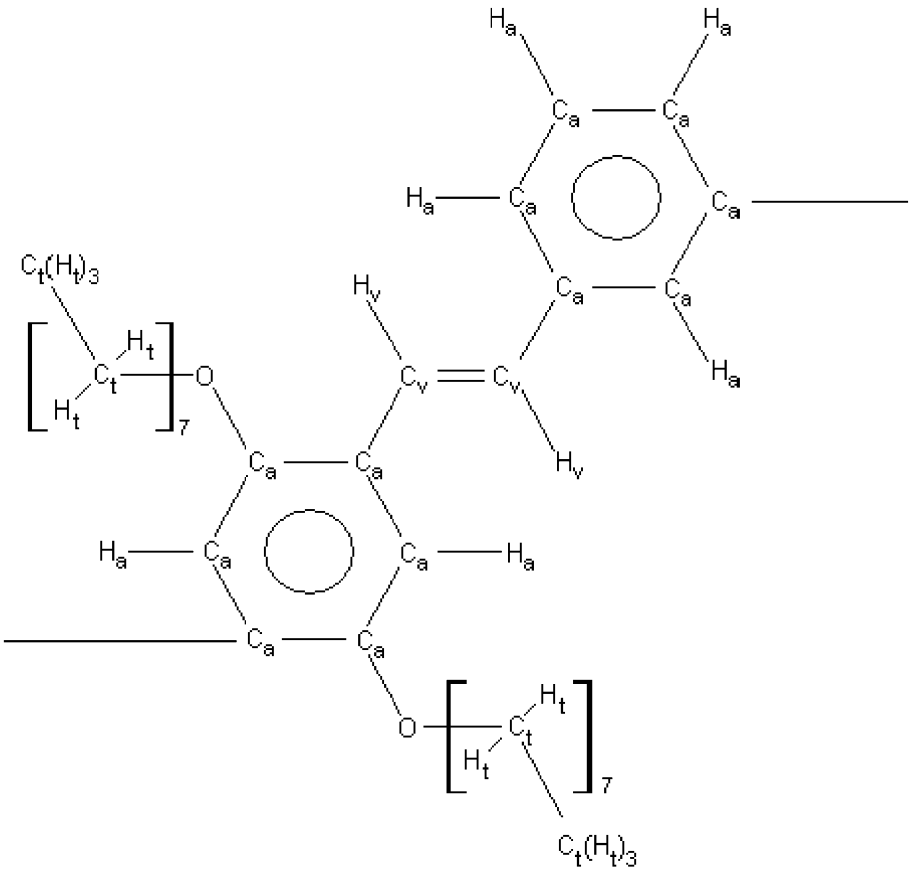

Fig. 1. PmPV molecular structure.

(AFM) observations revealed an average SWNT radius and length of approximately 0.7 nm and 3000 nm, respectively. The diamine and dianhydride used to synthesize the LaRC-CP2 were 1,3-bis(3-aminophenoxy) benzene (APB) and 2,2-bis(3,4-anhydrodicarboxyphenyl) hexafluoropropane (6FDA), respectively. As-received anhydrous dimethyl formamide (DMF) was used as a solvent. The details of the synthesis are described elsewhere [18].

A dilute SWNT solution, typically around 0.05% weight fraction in DMF, was prepared by homogenizing for 10 min (750 rpm with a 6 mm diameter rotor homogenizer) and sonicating for an hour at 47 kHz. In addition, a sample of purified SWNTs was additionally treated with an acid mixture in order to study the effect of additional SWNT treatment on the dispersion of nanotubes. The acid mixture was prepared in a round-bottom flask with concentrated H_2SO_4 and HNO_3 in the ratio of 3 to 1. The purified SWNT was added into the acid mixture and refluxed at 70 °C for 30 min to make a dark brown solution. The dark solution was diluted with distilled water and allowed to settle overnight. A

Table 1
Bond stretching parameters

Bond stretching	P (Å)	K^p (kcal/mol/Å^2)
C_t–C_t	1.529	268.0
C_t–H_t	1.090	340.0
C_t–O	1.415	201.4
C_a–O	1.355	431.6
C_a–C_a	1.400	469.0
C_a–H_a	1.080	367.0
C_a–C_v	1.320	520.0
C_v–C_v	1.320	520.0
C_v–H_v	1.080	367.0

Table 2
Bond-angle variation parameters

Bond-angle variation	Θ (°)	K^θ (kcal/mol/rad^2)
C_t–C_t–C_t	112.7	58.4
C_t–C_t–H_t	110.7	37.5
C_t–C_t–O	107.5	59.7
H_t–C_t–H_t	107.8	33.0
H_t–C_t–O	108.9	59.0
C_v–C_v–H_v	120.0	40.0
C_v–C_v–C_a	120.0	50.0
H_v–C_v–H_v	120.0	40.0
H_v–C_v–C_a	120.0	40.0
C_v–C_a–C_a	120.0	50.0
C_a–C_a–C_a	120.0	63.0
C_a–C_a–H_a	120.0	35.0
C_a–C_a–O	121.9	43.2
C_t–O–C_a	108.9	49.6

Table 3
Van der Waals interaction parameters

Van der Waals interaction	D^{I} (kcal/mol)	ρ^{I} (Å)
C_t	0.066	3.50
H_t	0.030	2.50
O	0.140	2.90
C_a	0.070	3.55
H_a	0.030	2.42
C_v	0.076	3.55
H_v	0.030	2.42

clear amber supernatant was decanted and the remaining dark solution containing the sediment was filtered through a sintered glass filter and washed thoroughly with distilled water and methanol under vacuum. A dried SWNT paper was peeled off from the filter and dried in a vacuum oven at 60 °C overnight. The acid-treated SWNT solution was also prepared as a dilute solution in DMF in the same manner described above. The sonicated SWNT solution was used as a solvent for the poly(amic acid) synthesis with the diamine and dianhydride. The entire reaction was carried out while stirring in a nitrogen-purged flask immersed in a 40 kHz ultrasonic bath until the solution viscosity increased and stabilized. Sonication was ceased and stirring was continued for several hours to form a SWNT-poly(amic acid) solution. Acetic anhydride and pyridine were added as catalysts with stirring to imidize the SWNT-poly(amic acid) chemically.

A series of SWNT/LaRC-CP2 nanocomposite films were prepared with a SWNT concentration of up to 1.0% nanotube weight fraction for both the as-received (which is the baseline system) and acid-treated systems. The SWNT-poly(amic acid) solution prepared was cast onto a glass plate and dried in a dry air-flowing chamber. Subsequently, the dried tack-free film was cured in a nitrogen-circulating oven to obtain solvent-free, free-standing SWNT–polyimide film. Examination of the films with Transmission Electron Microscopy and an optical microscope revealed that thin SWNT bundles were dispersed uniformly throughout the whole polymer matrix [18].

3. Molecular potential energy

The bonded and non-bonded interactions of the atoms in a molecular structure can be quantitatively described by using molecular mechanics. The forces that exist for each bond, as a result of the relative atomic positions, are described by the force field such that these forces contribute to the total molecular potential energy of a molecular system. The molecular potential energy for a nano-structured material is subsequently described by the sum of the individual energy contributions in the molecular model (Fig. 2). The individual energy contributions are summed over the total number of corresponding interactions in the molecular model. Various functional forms may be used for these energy terms depending on the particular material and loading conditions considered [19].

In the present study, the total molecular potential energy of the molecular model is taken to be:

$$\Lambda^{m} = \sum_{a} K_a^{\rho}(\rho_a - P_a)^2 + \sum_{a} K_a^{\theta}(\theta_a - \Theta_a)^2 + \sum_{a} D_a^{IJ}\left[\frac{1}{2}\left(\frac{\rho_a^{IJ}}{\rho_a}\right)^{12} - \left(\frac{\rho_a^{IJ}}{\rho_a}\right)^{6}\right] \quad (1)$$

where the terms P_a and Θ_a refer to the undeformed interatomic distance of bond number a and the undeformed bond-angle number a, respectively. The quantities ρ_a and θ_a are the distance and bond-angle after stretching and angle variance, respectively. The symbols K_a^{ρ} and K_a^{θ} represent the force constants associated with the stretching and angle variance of bond and bond-angle number a, respectively. The well depth and natural van der Waals distance for interaction a are given by, respectively [19]:

$$D_a^{IJ} = \sqrt{D_a^{I} \cdot D_a^{J}}$$
$$\rho_a^{IJ} = \sqrt{\rho_a^{I} \cdot \rho_a^{J}} \quad (2)$$

where the superscripts I and J denote the two atoms involved in an individual van der Waals interaction. Only the bond stretching, bond-angle variation, and van der Waals parameters were considered in Eq. (1) because other energy terms were found to have a negligible contribution to the total molecular potential energy. The values of the force constants, well depths, natural van der Waals distances, equilibrium bond lengths, and equilibrium bond angles associated with the Carbon, Hydrogen, and Oxygen atoms shown in Fig. 1 are listed in Tables 1–3.

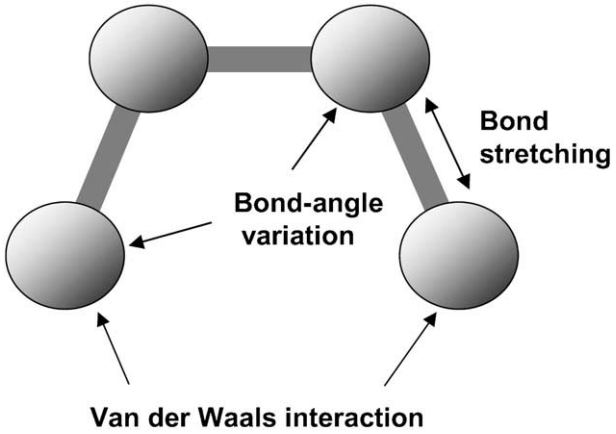

Fig. 2. Molecular mechanics modeling.

4. Molecular dynamics simulation

Molecular dynamics (MD) simulation has become an effective tool for studying the physics of condensed matter systems in which the forces acting on particles in a defined cell are calculated and the classical Newtonian equations of motion are integrated numerically [20–22]. In general, each particle is allowed to interact with all the other particles in the simulation.

In the present study, a MD simulation was used to generate the equilibrium structure of the composite system, which consisted of a (6,6) single-walled nanotube and five PmPV oligomers, each ten repeating units in length. The initial structure was constructed by placing the nanotube at the center of the MD cell, and by inserting the PmPV molecules at random, non-overlapping positions within the MD cell. This sample was equilibrated for approximately 500 ps at 800 K and 500 atm of hydrostatic pressure to relax the initial configuration and compress the system to an appropriate density. This initial procedure was followed by an additional 500ps of simulation at 300 K and 1 atm of pressure. By the end of the final equilibration run, the total energy and density had stabilized. No constraints were placed on the periodic MD cell shape or size.

The parameters used in the MD simulation are listed in Tables 1–3, with the atom labels defined in Fig. 1. All parameters, other than those involving the oxygen atom were taken from the OPLS-AA force field developed by Jorgensen and coworkers [23–25]. Parameters for the ether linkage were adapted from the MM3 force field [26–28]. All simulations were carried out with the TINKER® 3.8 [29] molecular modeling package and were performed in the constant NPT ensemble, using the Berendsen weak-coupling method to maintain the temperature and pressure near their specified values [30]. A modified Beeman integration algorithm, as implemented in the Tinker 3.8 package, was used to integrate the equations of motion [29]. The resulting molecular model is shown on the left side of Fig. 3.

5. Equivalent-continuum modeling

The equivalent-continuum model of the composite material can be developed based on the equilibrium molecular structure obtained with the MD simulation by using the methods of Odegard et al. [6]. This approach relies on an equivalent-continuum modeling technique that is used to predict the bulk mechanical behavior of nano-structured materials. The method consists of two major steps. First, a suitable representative volume element (RVE) of the nano-structured material is chosen. The RVE of a typical nano-structured material is on the nanometer length scale, therefore, the material of the RVE is not continuous, but is an assemblage of many atoms. Interaction of these atoms is described in terms of molecular mechanics force constants, which are known for most atomic structures [19]. In the second step, an equivalent-continuum model of the RVE is developed in which the

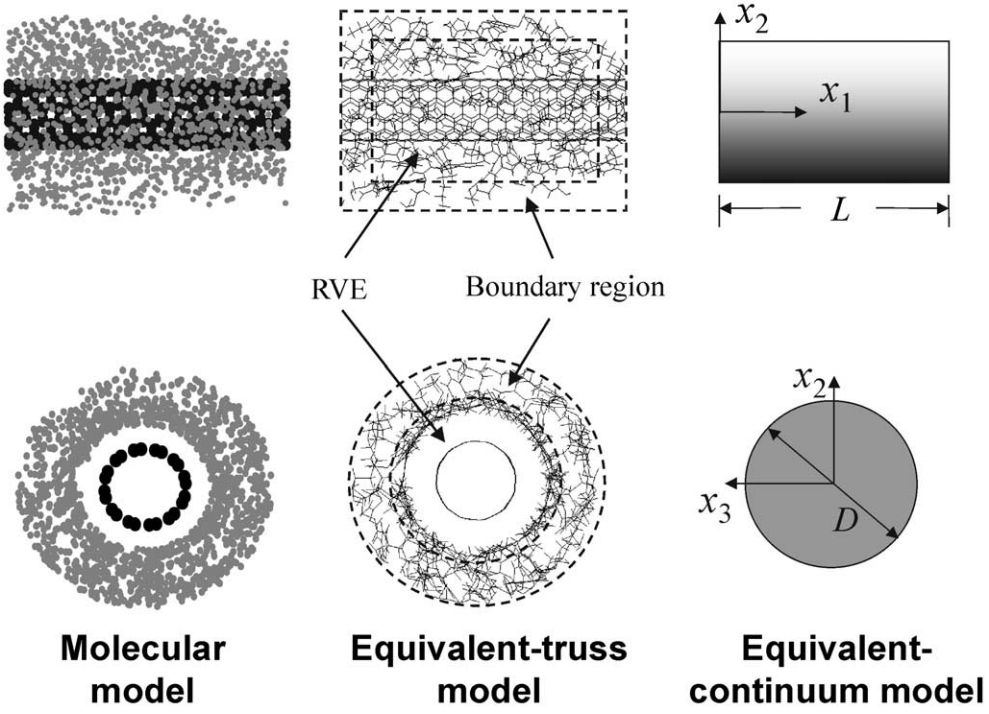

Fig. 3. Equivalent-continuum modeling of effective fiber.

total strain energies in the molecular and equivalent-continuum models, under identical loading conditions, are set equal. The effective mechanical properties, or the effective geometry, of the equivalent-continuum is then determined from equating strain energies.

For the most general approach, an equivalent-truss model of the RVE may be developed as an intermediate step to link the molecular and equivalent-continuum models. Each atom in the molecular model is represented by a pin-joint, and each truss element represents an atomic bonded or non-bonded interaction. The moduli of the truss elements are based on the molecular-mechanics force constants. Therefore, the total molecular potential energy of the molecular model and the strain energy of the equivalent-truss are equal for the same loading conditions.

5.1. Truss model

In traditional molecular models, the atomic lattice has been viewed as an assemblage of discrete masses that are held in place with atomic forces that resemble elastic springs [31]. The mechanical analogy of this model is a pin-jointed truss model in which each truss member represents either a bonded or non-bonded interaction between atoms. Therefore, the truss model allows the mechanical behavior of the nano-structured system to be accurately modeled in terms of displacements of the atoms. The deformation of each bonded or non-bonded interaction corresponds to the axial deformation of the corresponding truss element.

The total mechanical strain energy, Λ^t, of the truss model is:

$$\Lambda^t = \sum_b \sum_a \frac{A_a^b E_a^b}{2R_a^b}\left(r_a^b - R_a^b\right)^2 \tag{3}$$

where A_a^b and E_a^b are the cross-sectional area and Young's modulus of rod a of truss member type b, respectively. The term $r_a^b - R_a^b$ is the stretching of rod a of truss member type b, where R_a^b and r_a^b are the undeformed and deformed lengths of the truss elements, respectively.

In order to represent the mechanical behavior of the molecular lattice model with the truss model, Eq. (3) must be equated with Eq. (1) in a physically meaningful manner. Both equations are the sum of energies for particular degrees of freedom. The main difficulty in the substitution is specifying Eq. (3), which has stretching terms only, for Eq. (1), which also has bond-angle variance and van der Waals terms.

It was shown by Odegard et al. [6] that for small deformations, the Young's moduli of the rods representing primary bonds and the bond-angle variance interactions may be determined as a function of the force constants:

$$E_a^\alpha = \frac{2K_a^\rho R_a^\alpha}{A_a^\alpha} \tag{4}$$

$$E_a^\beta = \frac{32K_a^\theta}{A_a^\beta R_a^\beta}\left(\sin\frac{\Theta_a}{2}\right)^2 \tag{5}$$

where K_a^ρ, K_a^θ, and Θ_a are the same parameters associated with Eq. (1), and the superscripts α and β indicate primary bonding and bond-angle variance interactions, respectively.

Upon examination of Eq. (1), it is clear that the energy associated with van der Waals interactions is highly non-linear with respect to interatomic distance. The determination of the Young's moduli of truss elements that represent van der Waals interactions is complicated by accounting for this non-linearity and the large range of values for the interatomic distance of the interacting atoms in an equilibrium configuration. Therefore, linear relationships for the Young's modulus, such as those given by Eqs. (4) and (5), are not realistic for the van der Waals interactions.

To address this problem, the energy associated with the van der Waals interaction given in Eq. (1) and the strain energy of a truss element given by Eq. (3) were equated. The Young's modulus that represents the mechanical stiffness of a van der Waals interaction is given by:

$$E_a^\omega = \frac{2\rho_a^{\mathrm{IJ}} D_a^{\mathrm{IJ}}}{A_a^\delta\left(\rho_a - \rho_a^{\mathrm{IJ}}\right)^2}\left[\frac{1}{2}\left(\frac{\rho_a^{\mathrm{IJ}}}{\rho_a}\right)^{12} - \left(\frac{\rho_a^{\mathrm{IJ}}}{\rho_a}\right)^6\right] \tag{6}$$

where the superscript ω indicates van der Waals bonding. Clearly, the Young's modulus is highly dependent on the interatomic spacing. However, because of the difficulty of assigning an individual Young's modulus value for every van der Waals interaction in a nano-structured material, discrete values of Young's modulus may be approximated for ranges of interatomic spacing for each combination of atoms based on Eq. (6). The process for establishing these ranges is discussed below.

To implement the resultant equivalent-truss structure, a finite element model was developed by using ANSYS® 6 [32] (Fig. 3). Each element (LINK8) was a three-dimensional pin-jointed truss element with six degrees of freedom (three displacement components on each end) that represented a single atomic interaction. Each node corresponded to an atom in the equilibrium structure of the molecular model. A total of 14,501 elements and 1818 nodes were used in the model.

5.2. Continuum model

With the equivalent-truss structure in place, the continuum model could be constructed. The geometry of the linear-elastic, homogeneous, equivalent-continuum

RVE was assumed to be cylindrical, similar to that of the molecular and truss models (Fig. 3). With this approach, the mechanical properties of the solid cylinder were determined by equating the total strain energies of the equivalent-truss and equivalent-continuum models under identical loading conditions. Examination of the molecular model revealed that it was accurately described as having transversely isotropic symmetry, with the plane of isotropy perpendicular to the long axis of the nanotube. There are five independent material parameters required to determine the entire set of elastic constants for a transversely isotropic material. Each of the five independent parameters may be determined from a single boundary condition applied to both equivalent-truss and equivalent-continuum models. Once the mechanical properties of the equivalent-continuum RVE are determined, then the model may be used in subsequent micromechanical analyses as an effective fiber. The method employed in this study was adapted from the approach used by Hashin and Rosen [33] to determine elastic properties for fiber reinforced composite materials.

5.2.1. Effective-fiber constitutive model

The constitutive relationship of the transversely isotropic equivalent-continuum RVE (which is referred to as the effective fiber throughout the remainder of the paper) is:

$$\sigma_{ij} = C^f_{ijkl}\varepsilon_{kl} \tag{7}$$

where σ_{ij} and ε_{kl} are the stress and strain components, respectively ($i,j = 1,2,3$), and C^f_{ijkl} are the elastic stiffness components of the effective fiber (denoted by superscript f). Alternatively, Eq. (7) can be simplified by using the usual contracted notation for the elastic stiffness components and transversely-isotropic symmetry:

$$\begin{aligned}
\sigma_{11} &= C^f_{11}\varepsilon_{11} + C^f_{12}\varepsilon_{22} + C^f_{12}\varepsilon_{33}\\
\sigma_{22} &= C^f_{12}\varepsilon_{11} + C^f_{22}\varepsilon_{22} + C^f_{23}\varepsilon_{33}\\
\sigma_{33} &= C^f_{12}\varepsilon_{11} + C^f_{23}\varepsilon_{22} + C^f_{22}\varepsilon_{33}\\
\sigma_{12} &= 2C^f_{44}\varepsilon_{12}\\
\sigma_{13} &= 2C^f_{44}\varepsilon_{13}\\
\sigma_{23} &= \left(C^f_{22} - C^f_{23}\right)\varepsilon_{23}
\end{aligned} \tag{8}$$

Five independent elastic properties may be chosen to describe the complete set of elastic stiffness components, namely, the elastic stiffness component, C^f_{11}, and four elastic parameters: transverse shear modulus, G^f_{T}, transverse bulk modulus (also known as the plane-strain bulk modulus), K^f_{T}, longitudinal shear modulus, G^f_{L}, and longitudinal Young's modulus, E^f_{L}. The four elastic parameters are related to the elastic stiffness components by:

$$\begin{aligned}
G^f_{\mathrm{T}} &= \frac{1}{2}\left(C^f_{22} - C^f_{23}\right)\\
K^f_{\mathrm{T}} &= \frac{1}{2}\left(C^f_{22} + C^f_{23}\right)\\
G^f_{\mathrm{L}} &= C^f_{44}\\
E^f_{\mathrm{L}} &= C^f_{11} - \frac{2C^{f2}_{12}}{C^f_{22} + C^f_{23}}
\end{aligned} \tag{9}$$

Conversely, the elastic stiffness components can be described in terms of the four elastic parameters:

$$\begin{aligned}
C^f_{44} &= G^f_{\mathrm{L}}\\
C^f_{22} &= G^f_{\mathrm{T}} + K^f_{\mathrm{T}}\\
C^f_{23} &= K^f_{\mathrm{T}} - G^f_{\mathrm{T}}\\
C^f_{12} &= \left[K^f_{\mathrm{T}}\left(C^f_{11} - E^f_{\mathrm{L}}\right)\right]^{\frac{1}{2}}
\end{aligned} \tag{10}$$

At this point, both the elastic parameters and the elastic stiffness components are unknown. These values are determined by applying five identical sets of boundary conditions to the equivalent-truss model and the effective fiber, and by subsequently equating the strain energies by adjusting the five independent elastic properties. Boundary conditions must be chosen to yield unique values for the independent elastic properties.

5.2.2. Boundary conditions

Five sets of boundary conditions were chosen to determine each of the five independent elastic properties such that a single property could be independently determined for each boundary condition. The displacements and tractions applied at the boundaries of the RVE are generalized, respectively, by:

$$u_i(B) = \varepsilon_{ij}x_j \tag{11}$$

$$T_i(B) = \sigma_{ij}n_j \tag{12}$$

where B is the bounding surface, x_j is defined in Fig. 3, and n_j are the components of the outward normal vector to B. The generalized total strain energy of the effective fiber is:

$$\Lambda^f = \frac{V}{2}\sigma_{ij}\varepsilon_{ij} = \frac{\pi D^2 L}{8}\sigma_{ij}\varepsilon_{ij} \tag{13}$$

where V, D, and L are the volume, diameter, and length of the effective fiber, respectively (Fig. 3). The boundary conditions and strain energies for each of the five independent elastic properties are described below.

5.2.2.1. Transverse shear modulus. For a pure transverse shear strain, e, applied to the boundary of the equivalent-truss RVE and the effective fiber, $\varepsilon_{23} = e/2$, with the remaining strain components equal to zero. From Eq. (11), the boundary displacements are:

$$u_1(B) = 0$$
$$u_2(B) = \frac{e}{2}x_3$$
$$u_3(B) = \frac{e}{2}x_2 \tag{14}$$

From Eq. (13), the total strain energy of the effective fiber is:

$$\Lambda^f = \frac{1}{8}\pi D^2 L G_{\mathrm{T}}^f e^2 \tag{15}$$

where D and L are the diameter and length of the effective fiber, respectively (Fig. 3). The effective fiber strain energy, Λ^f, is equated to the strain energy of the truss subjected to the boundary conditions in Eq. (14). Since D and L are known, and e is arbitrarily chosen in determining Λ^f (in the range of small deformations, i.e. $e \ll 1$), then the transverse shear modulus of the effective fiber is directly evaluated from Eq. (15).

5.2.2.2. Transverse bulk modulus. The transverse bulk modulus was obtained in a similar manner by prescribing transverse strains $\varepsilon_{22} = \varepsilon_{33} = e$ to the RVE boundary with all remaining strain components set to zero. From Eq. (11), the displacements are:

$$u_1(B) = 0$$
$$u_2(B) = ex_2$$
$$u_3(B) = ex_3 \tag{16}$$

The strain energy of the effective fiber for this case is:

$$\Lambda^f = \frac{1}{2}\pi D^2 L K_{\mathrm{T}}^f e^2 \tag{17}$$

The transverse bulk modulus was determined from Eq. (17).

5.2.2.3. Longitudinal shear modulus. The longitudinal shear modulus was determined by prescribing a pure shear strain in the $x_1 - x_2$ plane, $\varepsilon_{12} = e/2$, with the remaining strain components set equal to zero. Therefore, the applied boundary displacements are:

$$u_1(B) = \frac{e}{2}x_2$$
$$u_2(B) = \frac{e}{2}x_1$$
$$u_3(B) = 0 \tag{18}$$

The resulting strain energy of the effective fiber is:

$$\Lambda^f = \frac{1}{8}\pi D^2 L G_{\mathrm{L}}^f e^2 \tag{19}$$

The longitudinal shear modulus was evaluated by using Eq. (19).

5.2.2.4. Longitudinal Young's modulus. The longitudinal Young's modulus was determined by prescribing a strain along the x_1 axis, $\varepsilon_{11} = e$, with all of the shear strain components set to zero. Since a transverse Poisson contraction is allowed in this case, the transverse normal stresses are set to zero, $\sigma_{22} = \sigma_{33} = 0$. From Eqs. (11) and (12), the boundary conditions are:

$$u_1(B) = ex_1$$
$$T_2(B) = 0$$
$$T_3(B) = 0 \tag{20}$$

The strain energy is:

$$\Lambda^f = \frac{1}{8}\pi D^2 L E_{\mathrm{L}}^f e^2 \tag{21}$$

The longitudinal Young's modulus was evaluated using Eq. (21).

5.2.2.5. Elastic stiffness component C_{11}^f. The elastic stiffness tensor component, C_{11}^f, may be determined by applying a strain parallel to the x_1 axis, while constraining the strains along the x_2 and x_3 axes, therefore preventing a Poisson contraction. For a prescribed strain, $\varepsilon_{11} = e$, with the remaining strains held at zero, the displacements from Eq. (11) are:

$$u_1(B) = ex_1$$
$$u_2(B) = 0$$
$$u_3(B) = 0 \tag{22}$$

From Eq. (13), the strain energy for these displacements is:

$$\Lambda^f = \frac{1}{8}\pi D^2 L C_{11}^f e^2 \tag{23}$$

Therefore, the elastic stiffness component C_{11}^f can be used as one of the five independent parameters that describe the overall properties of the transversely isotropic effective fiber.

5.2.3. Boundary region

The displacements and tractions specified above were applied to each node in the boundary region of the equivalent-truss model (indicated in Fig. 3), and the corresponding strain energies were calculated by summing the strain energies of each individual truss member in the RVE.

To determine the size of the boundary region, it was assumed that the range of the boundary region is related to the interatomic distance between the minimum nonbonded spacing found in the equilibrium structure and the maximum distance for which a positive-definite relationship exists between the force and displacement. It was also assumed that the contribution of the energies

associated with van der Waals forces between atoms with a separation distance larger than this maximum were relatively small and could be neglected.

The recent MD simulation of a SWNT surrounded by polyethylene molecules performed by Wise and Hinkley [5] predicted that the local changes in the polymer molecular structure and the non-functionalized SWNT/polymer interface are on the same length scale as the width of the nanotube. This recent study and the aforementioned assumptions led to the selection of a cylindrical boundary region that extends from a radius of 0.9 nm measured from the center of the nanotube to the outer edge of the molecular model (Fig. 3). Within the 0.9 nm radius, the RVE includes the nanotube, nanotube/polymer interface, and polymer molecules immediately adjacent to the interface.

5.2.4. Material property summary

The five independent parameters and the resulting stiffness tensor components, from Eq. (10), were determined for an effective fiber diameter, D, of 1.8 nm, length, L, of 3.2 nm, and applied strain, e, of 0.1%. These values are listed in Table 4.

6. Micromechanical analysis

The effective fiber accurately accounts for the structure–property relationships at the nanoscale and provides a bridge to the continuum model. With this process firmly established, constitutive models of the effective fiber/polymer composite may be developed with a micromechanical analysis by using the mechanical properties of the effective fiber and the bulk polymer matrix material. For the composite considered in this study, the PmPV molecules that were near the polymer/nanotube interface were included in the effective fiber, and it was assumed that the matrix polymer surrounding the effective fiber had mechanical properties equal to those of the bulk LaRC-SI and LaRC-CP2 resin. Because the bulk polymer molecules and the polymer molecules included in the effective fiber are physically entangled, perfect bonding between the effective fiber and the surrounding polymer matrix was assumed.

To address scale-up, the micromechanics-based Mori–Tanaka method [34] was used to predict the elastic stiffness properties of the effective fiber/polymer composite material. This method has been successfully applied to transversely-isotropic inclusions by Qui and Weng [35] and for this current method, the complete elastic stiffness tensor for the composite is given by Benveniste [36]

$$\mathbf{C} = \mathbf{C}^m + v_f\langle(\mathbf{C}^f - \mathbf{C}^m)\mathbf{A}^f\rangle\langle v_m\mathbf{I} + v_f\langle\mathbf{A}^f\rangle\rangle^{-1} \tag{24}$$

where v_f and v_m are the fiber and matrix volume fractions, respectively, $\mathbf{I}$ is the identity tensor, $\mathbf{C}^m$ is the stiffness tensor of the matrix material, $\mathbf{C}^f$ is the stiffness tensor of the fiber, and $\mathbf{A}^{\mathrm{f}}$ is the dilute mechanical strain concentration tensor for the fiber

$$\mathbf{A}^f = \left[\mathbf{I} + \mathbf{S}(\mathbf{C}^m)^{-1}(\mathbf{C}^f - \mathbf{C}^m)\right]^{-1} \tag{25}$$

The tensor $\mathbf{S}$ is Eshelby's tensor, as given by Eshelby [37] and Mura [38]. The terms enclosed with angle-brackets in Eq. (24) represent the average value of the term over all orientations defined by transformation from the local fiber coordinates (x_1, x_2, x_3) to the global coordinates (x_1''', x_2''', x_3''') (Fig. 4). For example, the transformed dilute mechanical strain concentration tensor for the fiber with respect to the global coordinates is

$$\bar{\mathbf{A}}^f_{ijkl} = c_{ip}c_{jq}c_{kr}c_{ls}\mathbf{A}^f_{pqrs} \tag{26}$$

where c_{ij} are the direction cosines for the transformation indicated in Fig. 4; that is,

$$\begin{aligned}
c_{11} &= \cos\phi\cos\psi - \sin\phi\cos\gamma\sin\psi\\
c_{12} &= \sin\phi\cos\psi + \cos\phi\cos\gamma\sin\psi\\
c_{13} &= \sin\psi\sin\gamma\\
c_{21} &= -\cos\phi\sin\psi - \sin\phi\cos\gamma\cos\psi\\
c_{22} &= -\sin\phi\sin\psi + \cos\phi\cos\gamma\cos\psi\\
c_{23} &= \sin\gamma\cos\psi\\
c_{31} &= \sin\phi\sin\gamma\\
c_{32} &= -\cos\phi\sin\gamma\\
c_{33} &= \cos\gamma
\end{aligned} \tag{27}$$

In general, the orientation average of the dilute mechanical strain concentration tensor is [39]

$$\langle\mathbf{A}^f\rangle = \frac{\int_{-\pi}^{\pi}\int_0^{\pi}\int_0^{\pi/2}\bar{A}^f(\phi,\gamma,\psi)\ \lambda(\phi,\psi)\ \sin(\gamma)\mathrm{d}\phi\mathrm{d}\gamma\mathrm{d}\psi}{\int_{-\pi}^{\pi}\int_0^{\pi}\int_0^{\pi/2}\ \lambda(\phi,\psi)\ \sin(\gamma)\mathrm{d}\phi\mathrm{d}\gamma\mathrm{d}\psi} \tag{28}$$

where $\lambda(\phi,\psi)$ is the orientation distribution function

$$\lambda(\phi,\psi) = \exp\left[-s_1\phi^2\right]\exp\left[-s_2\psi^2\right] \tag{29}$$

and where s_1 and s_2 are factors that control the orientation. Three cases considered in this paper are

Table 4
Effective-fiber independent parameters and elastic stiffness components (GPa)

$G^f_{\mathrm{T}} = 4.4$	$C^f_{11} = 457.6$
$K^f_{\mathrm{T}} = 9.9$	$C^f_{12} = 8.4$
$G^f_{\mathrm{L}} = 27.0$	$C^f_{22} = 14.3$
$E^f_{\mathrm{L}} = 450.4$	$C^f_{23} = 5.5$
	$C^f_{44} = 27.0$

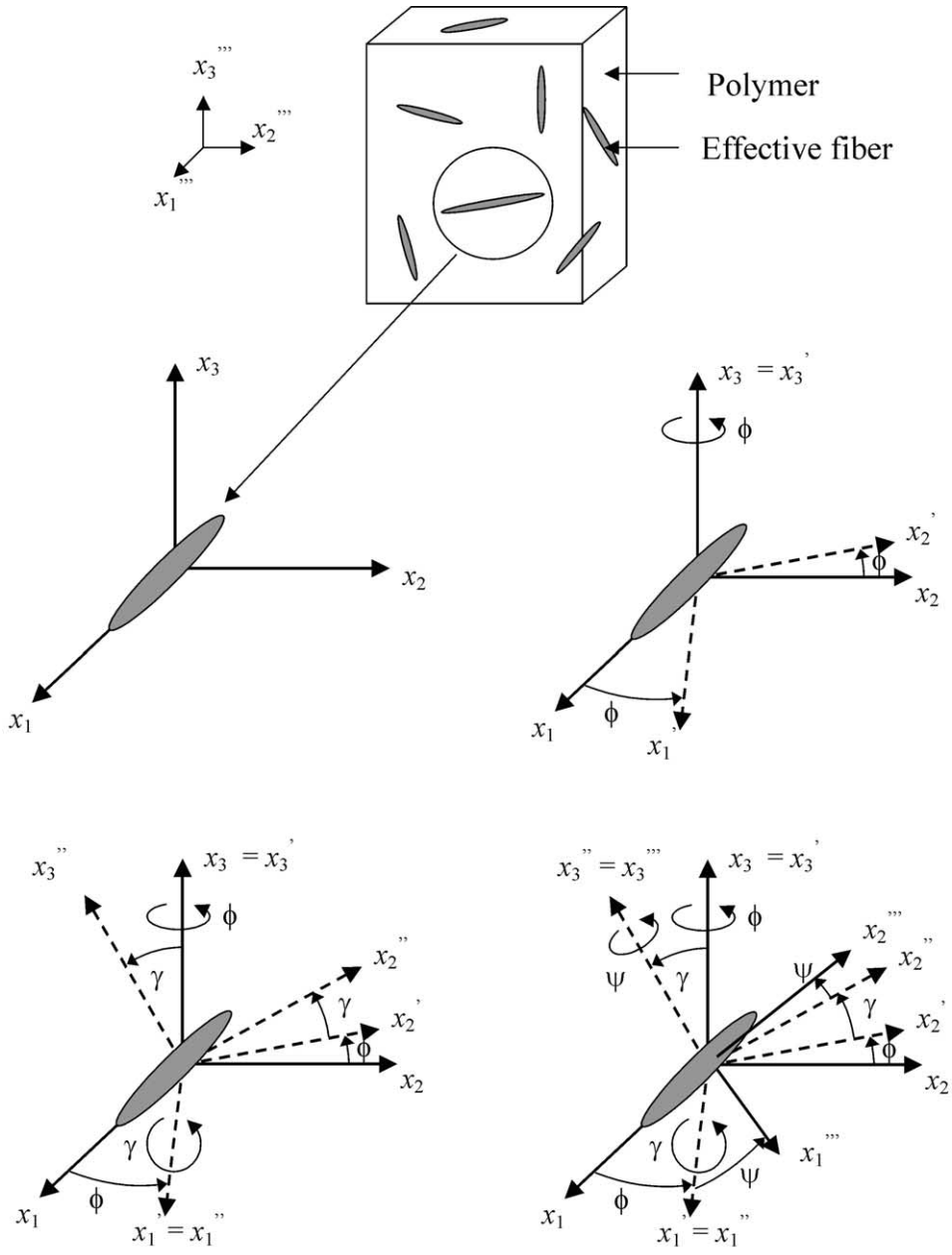

Fig. 4. Effective-fiber orientation.

$$\begin{array}{ll} \text{random} : s_1 = 0, \;\; s_2 = 0 & \lambda(\phi,\psi) = 1 \\ \text{aligned} : s_1 = \infty, \;\; s_2 = \infty & \lambda(\phi,\psi) = \\ & \quad \delta(\phi - 0)\delta(\psi - 0) \\ \text{axisymmetric} : \;\; s_1 = k, s_2 = \infty & \lambda(\phi,\psi) = \\ & \quad \exp\left[-k\phi^2\right]\delta(\psi - 0) \end{array} \tag{30}$$

where $\delta(y - \bar{y})$ is Dirac's delta distribution, centered at $\bar{y}$. The random case is a completely randomly oriented composite (i.e. randomly oriented in three dimensions). The aligned case corresponds to fibers perfectly aligned along the x_1''' axis. The axisymmetric case is an axisymmetric distribution of fibers about the x_1''' axis. The constant k describes the relative amount of alignment of the fibers with respect to the x_1''' axis. For large values of k ($k \to \infty$), the axisymmetric distribution approaches the aligned case, and for small values of k ($k \to 0$), the fibers are axisymmetrically distributed over all values of the angle ϕ with respect to the x_1''' axis. A plot of the orientation distribution functions for various intermediate values of k is shown in Fig. 5.

For the effective fiber/polymer composites considered in this study, the elastic stiffness components, volume fraction, length, and orientation of the effective fiber were used for the fiber properties in Eqs. (24) and (25). The effective fibers were assumed to have a spheroidal geometry for the Eshelby tensor in Eq. (25). The triple

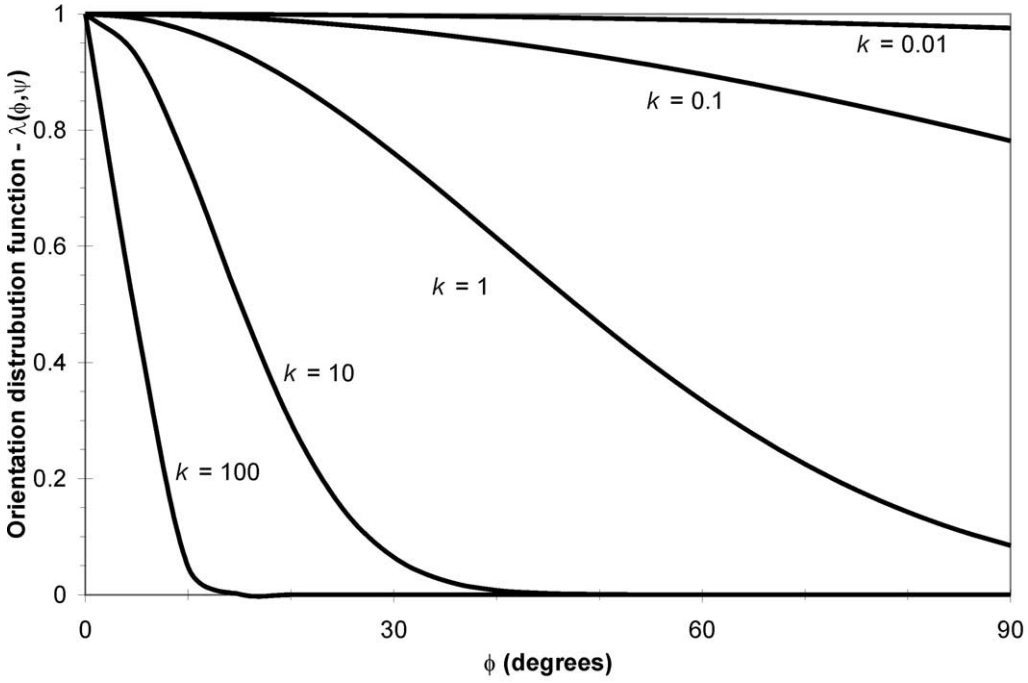

Fig. 5. Orientation distribution function for various values of the alignment factor k.

integral in Eq. (28) was evaluated numerically by using the extended trapezoidal rule [40].

7. Results

7.1. SWNT/LaRC-SI composite

In this section, the moduli of the effective-fiber/polymer composite are presented in terms of nanotube length, volume fraction, and orientation distribution. While the nanotube and effective-fiber lengths are equal, the nanotube volume fraction was determined to be 34% of the effective-fiber volume fraction if it is assumed that the nanotube volume is a hollow cylinder with a wall thickness equal to interatomic spacing of graphene sheets (0.34 nm). The properties of the composite with randomly and axisymmetrically oriented nanotubes were calculated for nanotube lengths up to 200 nm. This maximum length was chosen based on the decreased likelihood of a typical nanotube remaining straight as the nanotube length exceeds 200 nm.

Fig. 6 is a plot of the calculated longitudinal Young's modulus, E_L, and longitudinal shear modulus, G_L, for the random, aligned, and axisymmetric composites as a function of nanotube length, for a 1% nanotube volume fraction. These quantities were calculated from the elastic-stiffness tensor of the composite, $\mathbf{C}$, by using Eq. (9) for the composite. The results indicate that there is an approximately 55% increase in the shear modulus of the randomly oriented nanotube composite in the range of nanotube lengths between 0 and 200 nm, with a significant change in the slope occurring between nanotube lengths of 50 and 100 nm. Conversely, the calculated longitudinal shear modulus for the aligned nanotube composite was constant for the given range of nanotube length. Therefore, under these conditions, increasing the degree of alignment resulted in a decrease in shear modulus.

From Fig. 6 it can be seen that there is about a 400% increase in the longitudinal Young's modulus for the aligned composite with nanotubes that are 200 nm long, with respect to the polymer system without reinforcement. The data also indicate that alignment of the nanotubes results in nearly a 300% increase in the longitudinal Young's modulus for the composite with nanotubes that are 200 nm long. Unlike the case for shear modulus, an increase in the degree of alignment resulted in an increase in the longitudinal Young's modulus. A significant decrease in the slope of the Young's-modulus curves occurs between nanotube lengths of 60–80 nm.

The longitudinal Young's modulus of the aligned composite is plotted in Fig. 7 as a function of nanotube volume fraction for nanotubes that are 10, 50, and 500 nm long. Young's modulus increases with an increase in volume fraction, with the most pronounced rate of increase associated with nanotubes of length 50 nm or greater. The dependence of the longitudinal Young's modulus on the nanotube volume fraction becomes more linear as the nanotube length increases. This dependence is expected because of the well-known effect of the increase in load transfer with subsequent increases in reinforcement length and volume fraction [41].

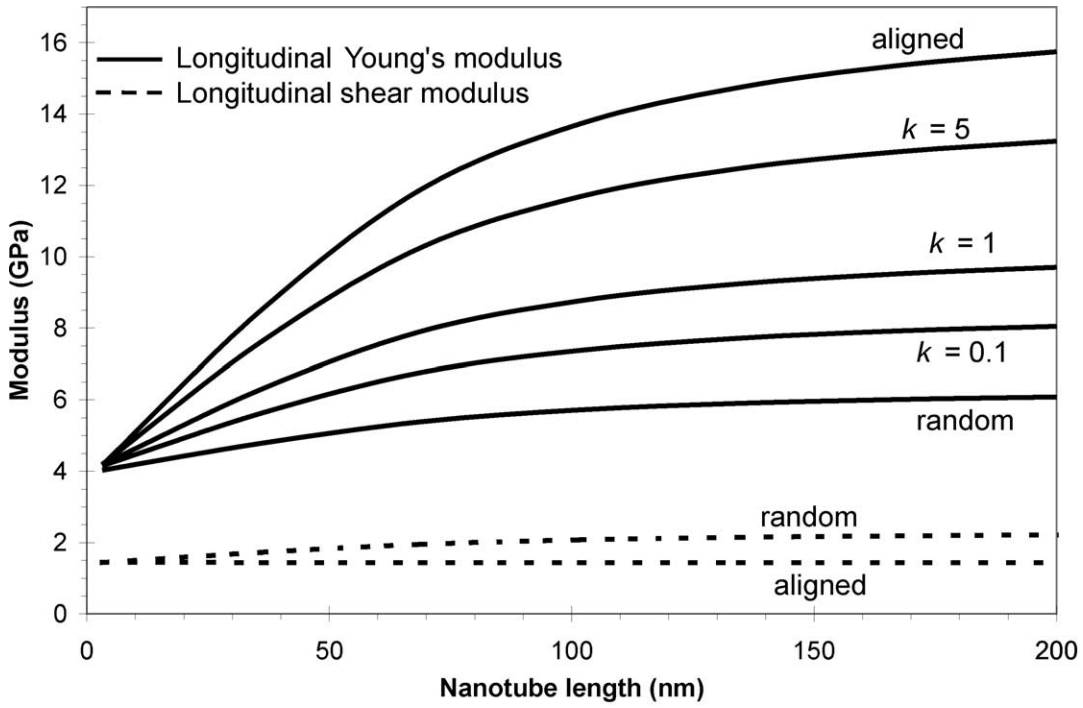

Fig. 6. Modulus of SWNT/LaRC-SI composite material vs. nanotube length for a 1% nanotube volume fraction.

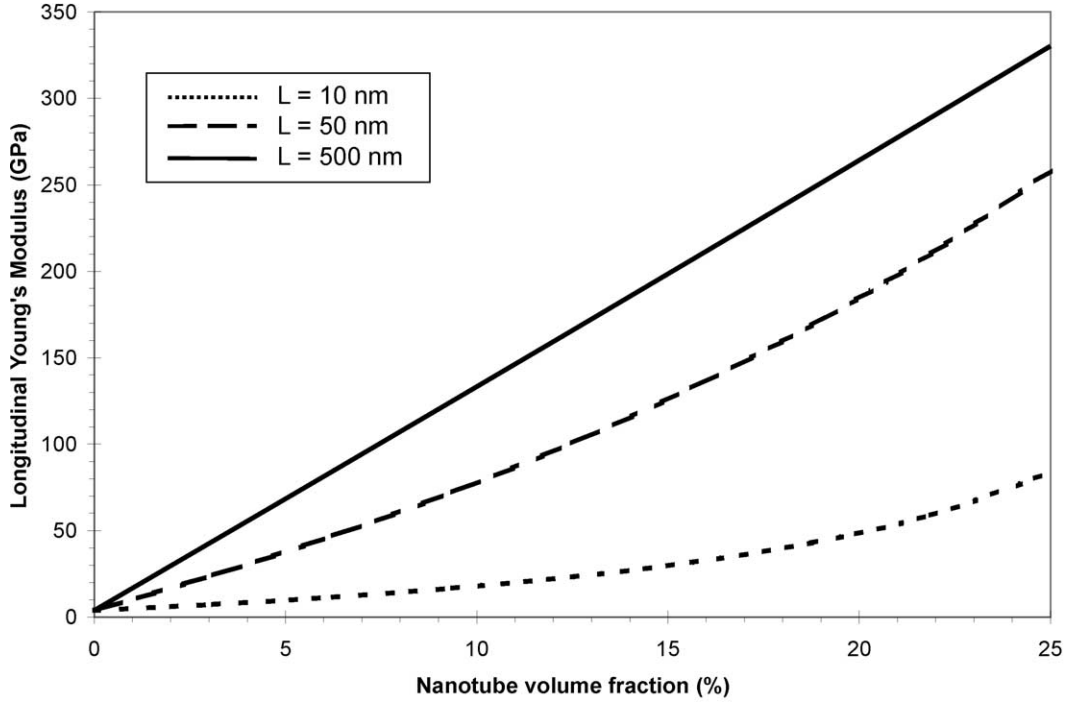

Fig. 7. Longitudinal Young's modulus of aligned SWNT/LaRC-SI composite vs. nanotube volume fraction.

For 500 nm long aligned nanotubes, the longitudinal Young's modulus of a composite with a 25% nanotube volume fraction is about 85 times larger than the Young's modulus of the un-reinforced resin.

Fig. 8 is a plot of the Young's modulus and the shear modulus for the random composite as a function of nanotube volume fraction, for three nanotube lengths. In general, an increase in nanotube volume fraction results in increased moduli values. For both the Young's and the shear moduli, increasing the volume fraction for the short nanotubes of length near 10 nm provides little to no improvement in stiffness. However, for nanotubes between 50 and 200 nm, equivalent stiffness can easily be obtained by trading off a decrease in

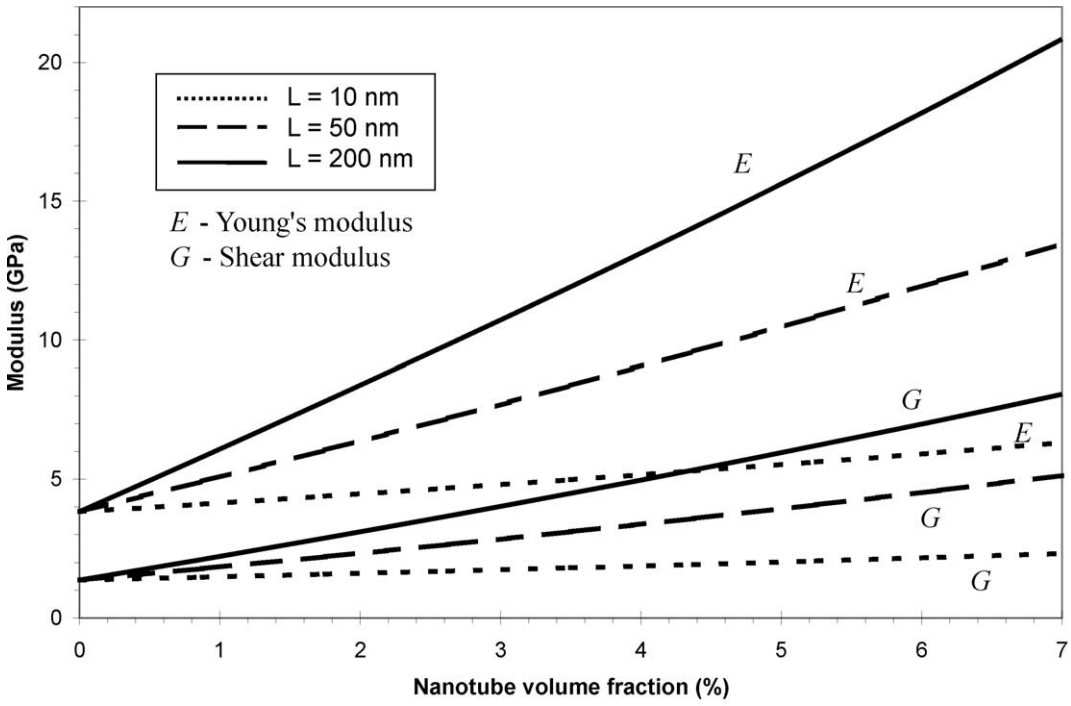

Fig. 8. Modulus of random SWNT/LaRC-SI composite material vs. nanotube volume fraction.

nanotube length for a small (2× or less) change in volume fraction. Increasing the nanotube length above 200 nm results in negligible increases in modulus.

The longitudinal Young's modulus for the axisymmetric composite is plotted in Fig. 9 as a function of nanotube volume fraction, for nanotubes that are 200 nm long. Three different values of k are shown. For comparison, the plots for a random and aligned composite are also shown for nanotubes that are 200 nm long. It is clear that the variation of the alignment factor k has a significant effect on the Young's modulus. As k increases and decreases, the longitudinal Young's modulus of the axisymmetric composite approaches that of the aligned composite and the random composite, respectively.

7.2. SWNT/LaRC-CP2 composite

In this section, the Young's modulus of the SWNT/LaRC-CP2 composite is determined as a function of nanotube volume fraction, and compared to experimentally determined values of Young's modulus. Mechanical properties of the films were evaluated by a Rheometrics dynamic mechanical analyzer (DMA). The film specimens had dimensions of 12 mm × 5 mm × 35 μm, and were dynamically loaded in tension at a constant frequency of 1 Hz. A plot of the experimental data is shown in Fig. 10 for the composite material prepared with both the as-received and acid-treated nanotubes. It is assumed that the Young's modulus is equal to the storage modulus obtained from the DMA at room temperature. Even though a total of three tests were performed for each data point, only one set of the data points is shown in Fig. 10 since the replicate values were nearly identical with the set shown. The conversion of nanotube weight fraction to nanotube volume fraction was performed by using the methodology of Pipes et al. [42]. It was assumed that the volume of the nanotube is defined as a solid cylinder with a radius equal to the sum of radius of the nanotube carbon atoms and half of the distance between the nanotube carbon atoms and the radius of the closest polymer atoms. It can be seen from Fig. 10 that the Young's modulus of the composite with acid-treated nanotubes is slightly larger than the composite with the as-received nanotubes.

The effective fiber properties determined in Section 7.1 were used to model the SWNT/LaRC-CP2 composite. The Young's modulus of the LaRC-CP2 neat resin was taken from the experimental data for a 0% nanotube volume fraction (0.85 GPa), and a typical value of Poisson's ratio for a polyimide was assumed (0.4). It was determined that the nanotube volume fraction was 37% of the effective fiber volume fraction if it is assumed that the nanotube volume is defined as stated above for the conversion of nanotube weight fraction to volume fraction. The properties of the composite material with randomly oriented nanotubes were calculated for nanotube lengths of 3000 nm. The predicted Young's modulus, as a function of nanotube volume fraction, is shown in Fig. 10. Even though there is good agreement between the model and the acid-treated

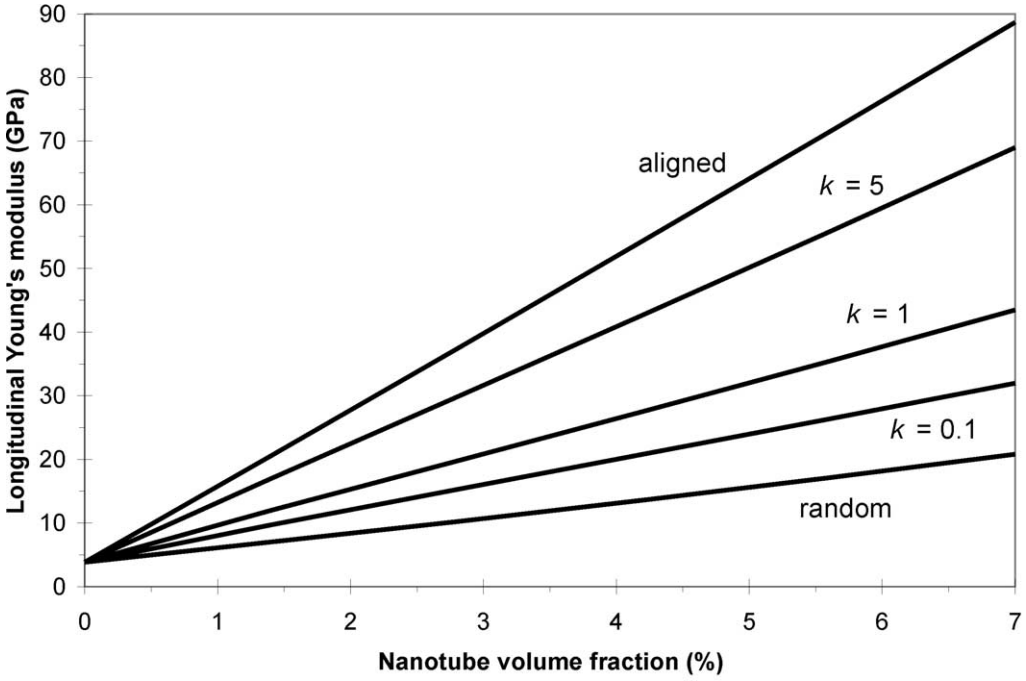

Fig. 9. Longitudinal Young's modulus of axisymmetric SWNT/LaRC-SI composite vs. nanotube volume fraction for nanotube lengths of 200 nm.

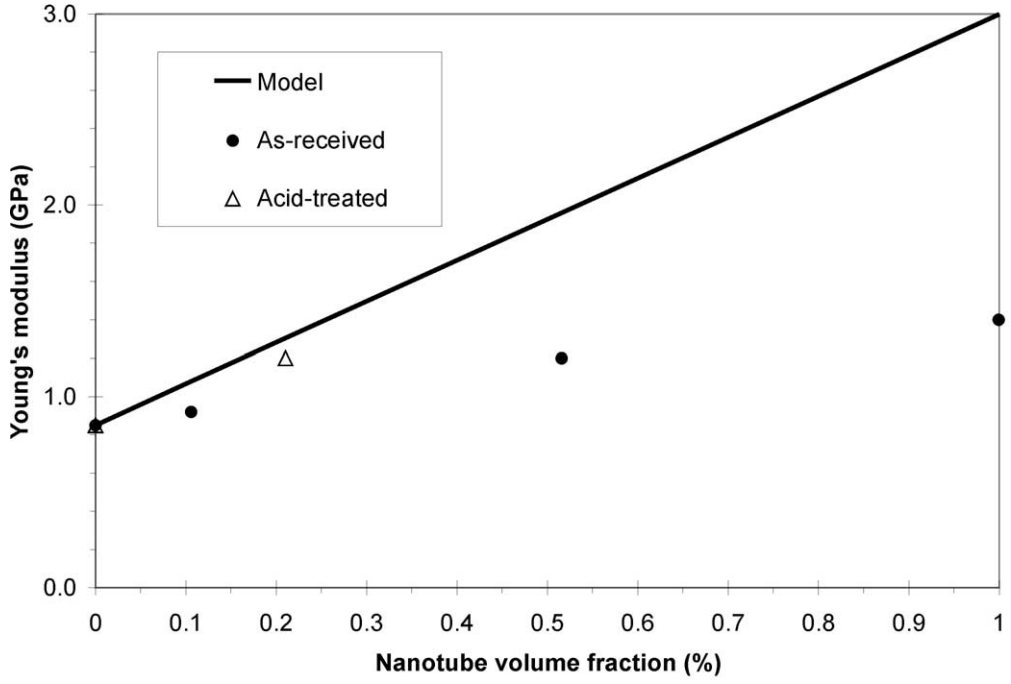

Fig. 10. Young's modulus of random SWNT/LaRC-CP2 composite vs. nanotube volume fraction.

nanotube composite, the predicted values of modulus are larger than the measured values for the as-received material, especially for values of nanotube volume fraction greater than about 0.5%. For example, at 0.21% nanotube volume fraction, the predicted Young's modulus is 12 and 35% higher than the measured values from the acid-treated and as-received materials, respectively. The difference between the experiments and the model is most likely caused by the fact that while the model assumes that the effective fibers are perfectly dispersed in the polymer matrix, a significant amount of nanotubes remain in bundles in the composite material, as shown by Park et al. [18]. The closer agreement between the model and the acid-treated values indicates

that the nanotubes are more dispersed in the acid-treated material than in the as-received material.

8. Summary and conclusions

In this study, a method has been presented for linking atomistic simulations of nano-structured materials to continuum models of the corresponding bulk material. For a polymer composite system reinforced with single-walled carbon nanotubes (SWNT), the method provides the steps whereby the nanotube, the local polymer near the nanotube, and the nanotube/polymer interface can be modeled as an effective continuum fiber by using an equivalent-continuum model. The effective fiber retains the local molecular structure and bonding information, as defined by molecular dynamics, and serves as a means for linking the equivalent-continuum and micromechanics models. The micromechanics method is then available for the prediction of bulk mechanical properties of SWNT/polymer composites as a function of nanotube size, orientation, and volume fraction. The utility of this method was examined by modeling SWNT/LaRC-SI and SWNT/LaRC-CP2 composites, both having a PmPV interface. The elastic stiffness constants of the SWNT/LaRC-SI composite were determined for both aligned and three-dimensional randomly oriented nanotubes, as a function of nanotube length and volume fraction. The Young's modulus of the SWNT/LaRC-CP2 composite was determined for the three-dimensionally randomly oriented nanotubes as a function of nanotube volume fraction.

For the SWNT/LaRC-SI composite at 1% nanotube volume fraction, stiffness will approach a maximum for nanotube lengths of 60–80 nm or greater for aligned, axisymmetric, and random nanotube orientations. Lengths above this range will also provide the most efficient increase in modulus for small changes in nanotube volume fraction. As length increases above this range, there is a limiting value such that small gains are realized for lengths above approximately 200 nm. This limiting value indicates that for nanotube lengths of approximately 200 nm, the efficiency of load transfer is nearly maximized. For long nanotubes (at least 200 nm), the relationship between stiffness and volume fraction is linear, which resembles the usual rule-of-mixtures approximation for long-fiber composites. For short, aligned nanotubes (10 nm), the volume fraction must exceed 10% before stiffness gains can be obtained. For randomly oriented nanotubes, measurable stiffness gains can be realized for small volume fractions.

For the SWNT/LaRC-CP2 composite with three-dimensionally randomly-oriented fibers, the Young's modulus is predicted to increase significantly for small volume fractions. Comparison with experiments suggests that these stiffness gains can only be achieved when the nanotubes no longer remain in their bundled form. The composite with the acid-treated nanotubes demonstrates a closer agreement with the model than the composite with the as-received nanotubes.

For many nano-structured materials, the trade-offs between structure and property must be established before the material can be optimized for any given application. The method presented in this paper provides a means for parametrically exploring these structure-property relationships. The method is applicable to a wide range of problems that require the accuracy of atomistic-level descriptions coupled with the general applicability of continuum-level models.

Acknowledgements

This work was partially performed while Dr. Odegard and Dr. Wise held National Research Council Research Associateship Awards at NASA Langley Research Center.

References

[1] McCullough RL. Micro-models for composite materials—continuous fiber composites. In: Whitney JM, McCullough RL, editors. Delaware composites design encyclopedia-volume 2: micromechanical materials modeling. Lancaster (PA): Technomic; 1990.

[2] McCullough RL. Micro-models for composite materials—particulate and discontinuous fiber composites. In: Whitney JM, McCullough RL, editors. Delaware composites design encyclopedia-volume 2: micromechanical materials modeling. Lancaster (PA): Technomic; 1990.

[3] Qian D, Dickey EC, Andrews R, Rantell T. Load transfer and deformation mechanisms in carbon nanotube-polystyrene composites. Applied Physics Letters 2000;76(20):2868–70.

[4] Shaffer MSP, Windle AH. Fabrication and characterization of carbon nanotube/poly(vinyl alcohol) composites. Advanced Materials 1999;11(11):937–41.

[5] Wise K, Hinkley J. Molecular dynamics simulations of nanotube-polymer composites. In: American Physical Society Spring Meeting, 12–16 April 2001, Seattle, WA.

[6] Odegard GM, Gates TS, Nicholson LM, Wise KE. Equivalent-continuum modeling of nano-structured materials. Composites Science and Technology 2002;62(14):1869–80.

[7] Iijima S. Helical microtubules of graphitic carbon. Nature 1991; 354:56–8.

[8] Edelstein AS, Cammarata RC. Nanomaterials: synthesis, properties and applications. Bristol: Institute of Physics Publishing; 1996.

[9] Dresselhaus MS, Dresselhause G, Eklund PC. Science of fullerenes and carbon nanotubes. San Diego: Academic Press; 1996.

[10] Frankland S J V, Caglar A, Brenner D W, Griebel M. Reinforcement mechanisms in polymer nanotube composites: simulated non-bonded and cross-linked systems. In: MRS Fall Meeting, Boston, MA, 2000.

[11] Chen RJ, Zhang Y, Wang D, Dai H. Noncovalent sidewall functionalization of single-walled carbon nanotubes for protein immobilization. Journal of the American Chemical Society 2001; 123:3838–9.

[12] Star A, Stoddart JF, Steuerman D, Diehl M, Boukai A, Wong EW, et al. Preparation and properties of polymer-wrapped single-walled carbon nanotubes. Angewandte Chemie International Edition in English 2001;40(9):1721–5.
[13] Nicholson LM, Whitley KS, Gates TS, Hinkley JA. Influence of molecular weight on the mechanical performance of a thermoplastic glassy polyimide. Journal of Materials Science 2000; 35(24):6111–22.
[14] Nicholson LM, Whitley KS, Gates TS. The combined influence of molecular weight and temperature on the physical aging and creep compliance of a glassy thermoplastic polyimide. Mechanics of Time-Dependent Materials 2001;5:199–227.
[15] Nicholson LM, Whitley KS, Gates TS. The role of molecular weight and temperature on the elastic and viscoelastic properties of a glassy thermoplastic polyimide. NASA/TM-2001-210664, 2001.
[16] Whitley KS, Gates TS, Hinkley J, Nicholson LM. Mechanical properties of LaRC™ SI polymer for a range of molecular weights. NASA/TM-2000-210304, 2000.
[17] St. Clair AK, St Clair TL, Slemp WS. Optically transparent/colorless polyimides. In: Weber W, Gupta M, editors. Recent advances in polyimide science and technology: characterization and applications. Poughkeepsie (NY): Society of Plastics Engineers; 1987.
[18] Park C, Ounaies Z, Watson KA, Crooks RE, Lowther SE, Connell JW. Dispersion of single wall carbon nanotubes by in situ polymerization under sonication. Chemical Physics Letters 2002; 364:303–8.
[19] Rappe AK, Casewit CJ. Molecular mechanics across chemistry. Sausalito (CA): University Science Books; 1997.
[20] Allen MP, Tildesley DJ. Computer simulation of liquids. Oxford: Oxford University Press; 1987.
[21] Rapaport DC. The art of molecular dynamics simulation. Cambridge: Cambridge University Press; 1995.
[22] Frankel D, Smit B. Understanding molecular simulation: from algorithms to applications. San Diego: Academic Press; 1996.
[23] Duffy EM, Kowalczyk PJ, Jorgensen WL. Do denaturants interact with aromatic hydrocarbons in water? Journal of the American Chemical Society 1993;115:9271–5.
[24] Jorgensen WL, Madura JD, Swenson CJ. Optimized intermolecular potential functions for liquid hydrocarbons. Journal of the American Chemical Society 1984;106:6638–46.
[25] Jorgensen WL, Severance DL. Aromatic–aromatic interactions: free energy profiles for the benzene dimer in water, chloroform, and liquid benzene. Journal of the American Chemical Society 1990;112:4768–74.
[26] Allinger NL, Yuh YH, Lii JH. Molecular mechanics. The MM3 force field for hydrocarbons. Journal of the American Chemical Society 1989;111:8551–66.
[27] Lii JH, Allinger NL. Molecular mechanics. The MM3 force field for hydrocarbons. 2. Vibrational frequencies and thermodynamics. Journal of the American Chemical Society 1989;111: 8566–75.
[28] Lii JH, Allinger NL. Molecular mechanics. The MM3 force field for hydrocarbons. 3. The van der Waals' potentials and crystal data for aliphatic and aromatic hydrocarbons. Journal of the American Chemical Society 1989;111:8576–82.
[29] Ponder JW. TINKER: software tools for molecular design, Ver. 3.8. Washington University School of Medicine; 1998.
[30] Berendsen HJC, Postma JPM, van Gunsteren WF, DiNola A, Haak JR. Molecular dynamics with coupling to an external bath. Journal of Chemical Physics 1984;81:3684–90.
[31] Born M, Huang K. Dynamical theory of crystal lattices. London: Oxford University Press; 1954.
[32] ANSYS, Ver. 6. Canonsburg (PA): SAS IP; 2001.
[33] Hashin Z, Rosen BW. The elastic moduli of fiber-reinforced materials. Journal of Applied Mechanics 1964;31:223–32.
[34] Mori T, Tanaka K. Average stress in matrix and average elastic energy of materials with misfitting inclusions. Acta Metallurgica 1973;21:571–4.
[35] Qui YP, Weng GJ. On the application of Mori–Tanaka's theory involving transversely isotropic spheroidal inclusions. International Journal of Engineering Science 1990;28(11):1121–37.
[36] Benveniste Y. A new approach to the application of Mori–Tanaka's theory in composite materials. Mechanics of Materials 1987;6:147–57.
[37] Eshelby JD. The determination of the elastic field of an ellipsoidal inclusion, and related problems. Proceedings of the Royal Society of London, Series A 1957;A241:376–96.
[38] Mura T. Micromechanics of defects in solids. The Hague: Martinus Nijhoff; 1982.
[39] Marzari N, Ferrari M. Textural and micromorphological effects on the overall elastic response of macroscopically anisotripic composites. Journal of Applied Mechanics 1992;59:269–75.
[40] Press WH, Flannery BP, Teukolsky SA, Vetterling WT. Numerical recipes. Cambridge: Cambridge University Press; 1986.
[41] Fukuda H, Takao Y. Thermoelastic properties of discontinuous fiber composites. In: Chou TW, editor. Comprehensive composite materials volume 1: fiber reinforcements and general theory of composites. New York: Elsevier; 2000.
[42] Pipes R B, Frankland S J V, Hubert P, Saether E. Self-consistent geometry, density and stiffness for the SWCN and its hexagonal arrays. NASA/CR-2002-212134, 2002.